A mathematical model of laser directed energy deposition for process mapping and geometry prediction of Ti-5553 single-tracks

M. Ansari , A. Martinez-Marchese , Y. Huang , E. Toyserkani

PII: S2589-1529(20)30127-7
DOI: https://doi.org/10.1016/j.mtla.2020.100710
Reference: MTLA 100710

To appear in: *Materialia*

Received date: 5 March 2020
Accepted date: 25 April 2020

Please cite this article as: M. Ansari , A. Martinez-Marchese , Y. Huang , E. Toyserkani , A mathematical model of laser directed energy deposition for process mapping and geometry prediction of Ti-5553 single-tracks, *Materialia* (2020), doi: https://doi.org/10.1016/j.mtla.2020.100710

A mathematical model of laser directed energy deposition for process mapping and geometry prediction of Ti-5553 single-tracks

M. Ansari[1], A. Martinez-Marchese[1], Y. Huang[2], E. Toyserkani[1*]

[1] *Multi-Scale Additive Manufacturing (MSAM) Lab, Department of Mechanical and Mechatronics Engineering, University of Waterloo, Waterloo, Ontario N2L 3G1, Canada*

[2] *Department of Mechanical Engineering, University College London, Torrington Place, London WC1E 7JE, United Kingdom*

Abstract

This research aims to develop a time-efficient physics-based model for laser directed energy deposition through coaxial powder feeding (LDED-CPF). A clear understanding of the interaction of the laser beam, powder, and substrate and its effects on the temperature field and geometrical characteristics of the melt pool, is of tremendous importance. This research first tries to analytically couple the moving laser beam, the powder stream, and the semi-infinite substrate. A process model is then developed for single-track deposition and experimental validation is conducted by depositing a titanium alloy (Ti-5553) at different laser powers and carrier gas flow rates. Moreover, an alternative method is established to estimate the deposit height based on the melt-pool projection and a process window is developed to consider more physics. Using the developed model, the processing parameters can be efficiently selected and the geometry and temperature field can be predicted for the single-track depositions.

Keywords: Additive manufacturing; Directed energy deposition; Analytical modeling; Process mapping; Temperature field; Geometry prediction

[*] Corresponding author.
E-mail address: ehsan.toyserkani@uwaterloo.ca (E.Toyserkani)

Nomenclature	
r_i, r_o	Nozzle tip outlet inner and outer radius, mm
r_l	Effective laser beam radius, mm
$\dot{V}$	Nozzle volumetric carrier gas flowrate, L/min
v_p	Particles velocity, mm/s
A_l	Cross-sectional area of laser-beam column, mm^2
A_{ps}	Cross-sectional area of powder-stream column, mm^2
A_p	Cross-sectional area of powder, mm^2
A_m	Area of the melt-pool projection on x-y plane, mm^2
A_d	Area of deposit on the y-z plane, mm^2
ξ	Powder efficiency of the nozzle
ρ_v	Mass concentration of powder per unit volume, g/mm^3
ε	Optical factor, mm^2/g
β_p	Absorption coefficient of powder
β_s	Absorptivity factor for the substrate
$\beta(\varphi)$	Absorptivity of an inclined surface
r_p	Powder average radius, mm
ρ	Density, g/mm^3
F	Powder feed rate, g/s
P_0	Initial power, W
$P_t(z)$	Transmitted or attenuated laser power in z-axis, W
L_{att}	Attenuation length, mm
N	Number of particles per unit time
m_p	Average mass of one powder particle, g
L_f	Latent heat of fusion, J/g
T_0	Ambient temperature, K
T_m	Melting temperature, K
v	Laser moving velocity, mm/s
k	Thermal conductivity, W/mmK
α	Thermal diffusivity, mm^2/s
c_p	Specific heat capacity, J/gK
φ	Inclination angle of melt-pool, degree
H	Deposit height, mm
W	Deposit width, mm
η	Catchment efficiency
δ	Heat diffusion depth, mm
t_i	Interaction time, s

1. Introduction

As defined by ASTM F2792-12a [1], directed energy deposition (DED) is categorized as one of metal additive manufacturing (AM) processes in which a focused heat source is used to directly deposit materials as they are being fed into the heat source. A further classification is provided as a function of the heat source (laser beam, electron beam, plasma, and electric arc), feedstock material (powder and wire), and feeding methods (off-axial and coaxial). In this article, we will use the nomenclature for laser (L), and coaxial (C) and off-axial (O) powder-fed (PF). In LDED-PF, the laser-powder interaction happens within the attenuation distance. The laser beam is attenuated by directly-injected powder particles and interacts with the underlying layer or substrate to form a melt-pool. Meanwhile, the heated powder particles reach the melt-pool and become a part of the melt-pool. Figure 1 shows the schematic of the LDED-CPF process. The melt-pool experiences rapid solidification while solidifying to form a track. Several physical phenomena contribute to the thermal characteristics, and geometry of the deposits.

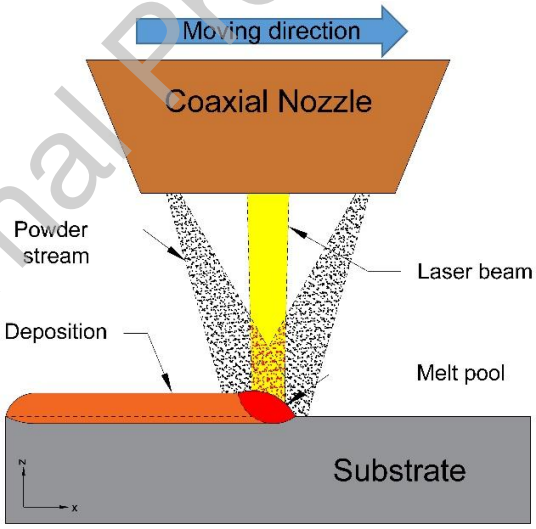

Figure 1. Scheme for LDED-CPF, showing the interaction of powder, laser beam, and substrate.

Any further development of LDED-PF requires a theoretical approach to shed more light on the interaction of powder particles, laser beam, and substrate. Then the heat and mass transfer should be coupled to advance the process modeling. The single-track deposition process, as the first step of the

process, should be optimized, and controlled for a stable deposition since an unstable deposition can undermine the quality and dimensional accuracy of the multi-track deposition process. Choosing optimum processing parameters would be challenging due to machine dependencies of many parameters such as the laser beam quality, powder stream profile, and particles velocity. The ultimate aim is to predict the processing parameters and the resultant deposit's geometry based on the basic aspects of the laser beam, powder stream, and thermophysical properties of the materials.

Different process modeling of LDED-PF, including analytical, numerical, and empirical/statistical, have been tried to address the above-mentioned challenges. Empirical/statistical models, which are developed based on the experimental data, have been extensively used for the single-track deposition optimization in LDED-PF, in general [2–8]. However, the empirical/statistical approach mainly considers a few variables as laser power, beam diameter, moving velocity, and powder feed rate. Each LDED-PF equipment has a different design for the nozzle, powder profile and laser beam and consequently, major physical phenomena would be affected by them. Physics-based modeling, including numerical and analytical modeling, is another approach. Physics-based models introduce intermediate variables from one stage of the process to the other. The complete deposition process can be broken down into several physical stages and each physical stage can have different variables [9]. Melt-pool forms as a result of the powder/laser/substrate interaction and the melt-pool characteristics define the final track properties. Figure 2 illustrates the physical stages and intermediate variables in LDED-PF.

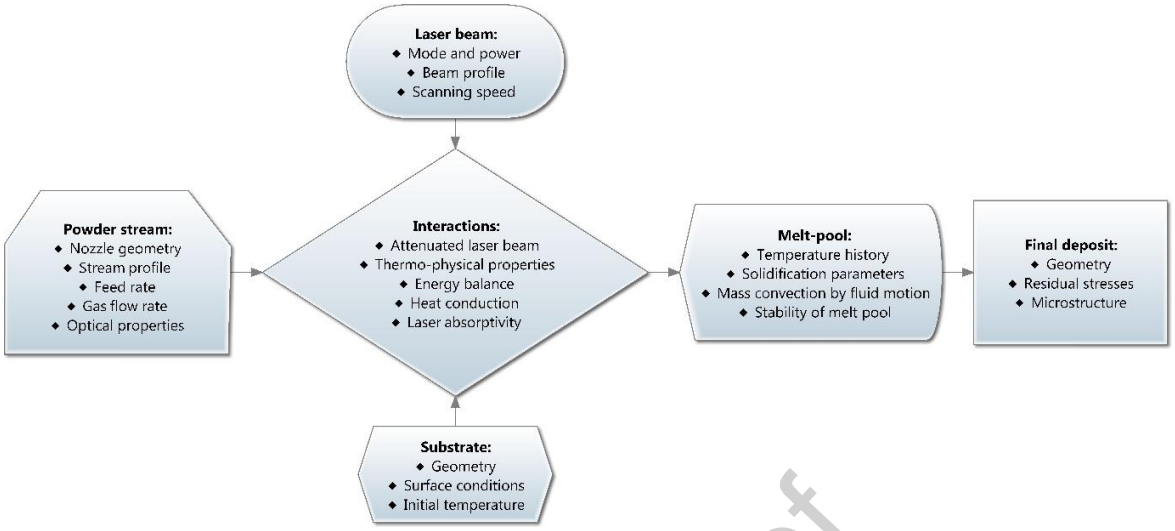

Figure 2. Physical stages and corresponding process variables in LDED-PF.

Numerical modeling has been verified as an accurate simulator for different aspects of the LDED-PF process such as powder flux distribution [10,11], laser-powder interaction [12], geometrical features of the deposit [13–16], temperature, fluid velocity fields [17,18]. However, the accuracy of numerical models is mainly governed by the discretization and meshing techniques, which significantly adds to the computational time and complexity of the model. Analytical modeling is a classic approach for understanding the basic physics of the LDED-PF process. Picasso et al. [19] developed a fundamental analytical model for the LDED-OPF process to predict the laser moving velocity and powder feed rate for a given set of parameters such as laser power, beam width, and powder stream geometry. Frenk et al. [20] proposed a quantitative analytical model for the LDED-OPF process based on the energy balance and overall mass to estimate the dimensions of melt-pool and deposit, as well as the catchment efficiency and global absorptivity. Lalas et al. [21] took an analytical approach for the LDED-OPF process to estimate the deposit geometry based on surface tension and taking into account the laser moving velocity and powder feed rate. Pinkerton et al. [22] integrated the powder stream and substrate thermal conduction and mass flow into an analytical model for LDED-CPF. Zhu et al. [23] established an alternative analytical model to estimate the geometric characteristics of the deposit based on the curve equation of the deposit, which takes into account the laser powder, laser-powder interaction. In the latest published study by

Huang et al. [24], a semi-analytical model developed for the LDED-OPF process. The paper tried to couple the heat flux and mass flow by considering the associated spatial distribution. However, this approach may increase the complexity of the model and computational time as it tries to calculate the attenuated laser power, the heated powder stream and the semi-infinite substrate based on the superposition of those functions. The accuracy of the analytical models for prediction is generally questionable since many simplified assumptions have been taken into account to compensate for the complexity of physics involved in the process. However, the analytical models can be a perfect fit for process mapping and parameter selection as they do not need a high accuracy prediction. There are a limited number of studies concerning an analytical approach for process mapping of the LDED-CPF process. As a preliminary model constructed on the basis of the attenuation of the laser beam by powder cloud, Jouvard et al. [25] adopted a very simple approach, taking into consideration Beer-Lambert law for the laser beam attenuation and a one-dimensional solution of the heat conduction, to define two thresholds for substrate and powder fusion. de Oliveira et al. [26] used the same approach to plot a brief process map showing the laser power required to melt the substrate and powder.

LDED-PF is still hampered in different degrees by poor quality and uncertainty of the final properties and geometry dimensions. The cause lies in the limited or unsuitable process models. A computationally fast and reliable model is needful. This research tries to analytically couple the heat and mass transfer during the process by covering more physical changes and considering some simplified assumptions in order to make the model more realistic, reliable, and time-efficient. Besides, an alternative method is established to estimate the deposit height and bead curvature based on the melt-pool projection on the substrate. The model only needs some simple characteristics of the powder stream and laser beam, and thermo-physical properties of the materials, which make it easy to apply the model to any materials/equipment of the same technology. The developed process model can be used to define preliminary processing parameters and it saves time and cost of doing screening-phase experiments. On

the other hand, the model is able to perform the geometry and temperature-field prediction for single-track depositions with acceptable accuracy.

2. Mathematical model

2.1. Laser/powder/substrate interaction

To keep a high fidelity of the developed model, the interaction among the laser beam, powder stream and substrate should be considered. As the laser beam heats the fast-moving particles and the substrate, it has to be quantified how much the beam is attenuated while passing through the powder cloud.

2.1.1. Particles velocity

To find the velocity of the particles, the first assumption is that there is a steady-state powder flow with constant velocity. The particles' pathway from the hopper to the nozzle is long enough such that the velocity of the particles can be assumed as equal as the gas flow speed. Then, the effects of drag force and gravity can be ignored. Having a nozzle tip with an annular outlet, and a fully coupled powder and gas flow, the average particles velocity (v_p) can be given by:

$$v_p = \frac{\dot{V}}{\pi\left[r_o^2 - r_i^2\right]} \qquad (1)$$

where r_i and r_o are the inner and outer radius of the outlet, respectively. $\dot{V}$ is the nozzle volumetric gas flowrate.

2.1.2. Attenuation of laser beam intensity by powder cloud

Quantifying the attenuated laser power needs the geometry of the powder stream and laser beam. Although the laser beam and powder stream both have a Gaussian intensity distribution in the transverse direction, it has been verified that a nearly uniform intensity distribution can be expected close to the focal position of the laser beam [27] and coaxial powder stream [12,28]. Then, it is well-accepted to consider an effective radius as it leads to the same effective area of the Gaussian and rectangular profiles.

The effective radius is the radius where the intensity criterion of $\frac{1}{e^3}$, $\frac{1}{e^2}$ or $\frac{1}{e}$ is applicable depending on the Gaussian mode. In this study, the intensity criterion of $\frac{1}{e}$ is considered to determine the effective radius of the powder stream and laser beam. Please note that the deposition should ideally happen where the focal position of the laser beam and coaxial powder stream locate close to each other on the substrate. Thus, for simplification of the modeling, the powder stream and laser beam close to their focal position are assumed as cylindrical columns with effective radii, and the depiction in Figure 3 would be acceptable, showing the powder stream and laser beam as cylindrical columns travelling coaxially along the x-axis. Other assumptions are as follows. The particle size distribution is uniform and particles have a spherical morphology. The effect of diffraction, reflection, and scattering of particles is assumed to be negligible. The particles do not overlap the others. The origin of the coordinate system is assumed at the center of the laser beam spot at the highest point of the deposition.

Since the cylindrical columns do not have the same size, the first ratio to define is the powder efficiency of the nozzle.

$$\xi = \frac{A_l}{A_{ps}} \qquad (2)$$

where, A_l and A_{ps} is the cross-section of laser beam and powder stream cylinders, respectively.

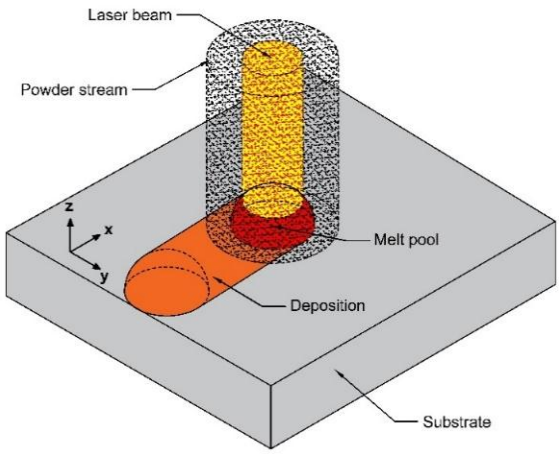

Figure 3. Geometric features of the powder stream and laser beam in the LDED-CPF process based on the simplified assumptions.

It has been proved that the Beer-Lambert law suffices to obtain the attenuation of a laser beam by a powder cloud [17,25,29,30]. The attenuation depends on the intensity of the incident beam, the concentration and nature of the powder cloud, and the attenuation length. Under the previously mentioned circumstances, the attenuated laser power intensity can be written as:

$$\frac{dI}{I(z)} = -\varepsilon \rho_v dz \qquad (3)$$

where, ρ_v is the mass concentration of powder per unit volume, and ε is an optical factor. Based on the theory of Mie [20], and the geometric optical law (considering scattering and absorption phenomena), the optical factor, as described by Jouvard et al. [25], is as follows:

$$\varepsilon = \frac{3R_p}{2r_p\rho_p} \qquad (4)$$

where, R_p is the reflectivity of powder $(1-\beta_p)$, β_p is the absorption coefficient of powder, r_p is powder average radius, and ρ_p is powder density.

For a powder stream with a cylindrical shape, uniform mass concentration, spherical-shape powder, and a constant particles velocity inside the powder stream column, the powder concentration is:

$$\rho_v = \frac{F}{A_{ps}v_p} \qquad (5)$$

where F is powder feed rate (g/s), v_p is particles velocity (mm/s) flying out of the nozzle, and A_{ps} is the cross-sectional area of the powder stream cylinder.

Finally, the laser beam power attenuation is given by:

$$\int_0^z \frac{dI}{I(z)} = \int_0^z \frac{-\varepsilon F}{A_{ps}v_p} dz$$

$$\ln I_t(z) - \ln I_0 = \ln \frac{I_t(z)}{I_0} = \frac{-\varepsilon F z}{A_{ps} v_p}$$

$$I_t(z) = I_0 exp\left(\frac{-\varepsilon F z}{A_{ps} v_p}\right)$$

$$P_t(z) = P_0 exp\left(\frac{-\varepsilon F z}{A_{ps} v_p}\right) \qquad (6)$$

where $P_t(z)$ is transmitted power or attenuated power within the attenuation distance of z, and P_0 is the initial power before attenuation.

2.1.3. Energy balance during the process

The laser energy absorbed by the substrate and powder during the attenuation time is added up and act as one energy source unit. Assuming a quasi-steady state was achieved during the LDED-PF process, the following energy balance should be fulfilled while ignoring the effect of latent heat of fusion, radiation, and convection [31]:

$$P_{Total}^{Deposition} = P_{Absorbed}^{Substrate} + P_{Absorbed}^{Powder} + P_{Absorbed\ by\ powder}^{Reflected\ by\ substrate} \qquad (7)$$

where the total power of deposition ($P_{Total}^{Deposition}$) is the sum of the power absorbed by the substrate ($P_{Absorbed}^{Substrate}$), power absorbed by the powder ($P_{Absorbed}^{Powder}$), and power reflected by the substrate and absorbed by powder ($P_{Absorbed\ by\ powder}^{Reflected\ by\ substrate}$).

The power released by the laser beam after its transmission through the powder cloud and getting absorbed by the substrate is:

$$P_{Absorbed}^{Substrate} = \beta_s P_t(z) = \beta_s P_0 exp\left(\frac{-\varepsilon F L_{att}}{A_{ps} v_p}\right) \qquad (8)$$

where, β_s is the absorptivity factor for the substrate.

As the nozzle injects the powder, particles interact with the laser beam within the attenuation distance and accumulate energy. The energy absorbed by one particle during the attenuation time is given by [25]:

$$dq_p = \frac{\beta_p A_p}{A_l} P_t(z) dt \qquad (9)$$

where, β_p is the absorptivity factor for the particles, and A_p is the cross-sectional area of the particle The attenuation time is a function of the attenuation length (L_{att}) and particles velocity, so we can write the energy based on the attenuation distance.

$$dt = \frac{dz}{v_p} \qquad (10)$$

Considering no convection and radiation losses, the energy absorbed by one particle is described as below.

$$q_p = \frac{\beta_p A_p}{A_l v_p} \int_0^{L_{att}} P_t(z) dz \qquad (11)$$

However, a number of particles are absorbing energy while they are flying. The number of particles per unit time is:

$$N = \frac{\xi F}{m_p} \qquad (12)$$

where, m_p is the average mass of a particle. The total power released by these particles is:

$$P_{Absorbed}^{Powder} = \frac{N \beta_p A_p}{A_l v_p} P_0 \int_0^{L_{att}} exp\left(\frac{-\varepsilon F z}{A_{ps} v_p}\right) dz \qquad (13)$$

On the other hand, the reflected part of the energy by the substrate would be again absorbed by the particles. The particles absorb the energy and transfer it back to the melt-pool. The reflected power by the substrate that is absorbed by particles is as follows:

$$P_{Absorbed\ by\ powder}^{Reflected\ by\ substrate} = \frac{N\beta_p A_p}{A_l v_p}(1-\beta_s)P_0 \int_0^{L_{att}} exp\left(\frac{-\varepsilon F z}{A_{ps} v_p}\right) dz \quad (14)$$

2.1.4. Heat conduction during the process

Assume that a stationary point heat source travels with a constant velocity along the x-axis. Then Rosenthal's solution for the quasi-steady-state temperature distribution on the surface of a semi-infinite plate is given as follows:

$$T_{ss}(x,y,z) = T_0 + \frac{P_{Total}^{Deposition}}{2\pi k R} e^{\frac{-v(x+R)}{2\alpha}} \quad (15)$$

$$R = \sqrt{x^2 + y^2 + z^2}$$

where, T_0 denotes the ambient temperature, $P_{Total}^{Deposition}$ denotes the total deposition power, v is the laser moving velocity, k and α denote the average thermal conductivity and diffusivity of powder and substrate material. The parameter R denotes the distance from the point of interest to the laser heat source. In order to cover more physical phenomena and make the model more realistic, some modified factors are taken into account.

In order to take the remelted zone of the substrate or dilution ratio (D) into consideration, it is assumed that the average contribution of the remelted zone to the melt-pool is 25 % ($D = 0.25$). The dilution ratio is usually between 0-50 percent, depending on the processing parameters, hence the average of 25 % would be reasonable.

$$\begin{cases} k = k_{powder}(1-D) + k_{substrate}(D) \\ c_p = c_{powder}(1-D) + c_{substrate}(D) \\ \rho = \rho_{powder}(1-D) + \rho_{substrate}(D) \\ T_m = T_m^{powder}(1-D) + T_m^{substrate}(D) \end{cases} \quad (16)$$

The effect of fluid motion (Marangoni effect) can be taken into consideration by a modified thermal conductivity [14,32].

$$k_t^* = \mu k_t, \quad T > T_m \qquad (17)$$

where μ is a correction factor for enhanced thermal conductivity. The correction factor has been reported to be between 2-5 depending on the material [32–34].

The absorptivity is related to the angle of incidence. The absorptivity of an inclined surface in the polarization plane is given as [35]:

$$\beta(\varphi) = \frac{4n_r cos\varphi}{(n_r cos\varphi + 1)^2 + {k_e}^2 cos^2\varphi} \qquad (18)$$

where φ is the inclination angle, n_r is refraction index, and k_e is the extinction index of the material. If the cross-section of the deposit is assumed to be a segment of a circle, the inclination angle is approximated as:

$$\varphi = \tan^{-1}\left(\frac{2H}{W}\right) \qquad (19)$$

where H is the deposit height and W is the deposit width. In order to make this simple, if the deposit forms a semicircle ($H = W/2$), then the inclination angle would be almost 45°. This can be also applied to the absorption coefficient of powder to compensate for the inclined plane because of the sphericity of particles, assuming that the laser beam gets reflected under the average angle of 45° due to the rounded shape of particles.

2.2. Melt-pool/deposit geometry

To get the geometry, the projection of the melt-pool on the substrate (x-y plane) is firstly needed. It can be approximately represented by the temperature distribution on the top surface of the substrate.

$$T(x, y, z) - T_0 = \Gamma(\mathrm{x}, \mathrm{y}, \mathrm{z}) \qquad (20)$$

Figure 4 shows the boundary of the melt-pool projection on different planes, as suggested by Huang et al. [24], and the following equations denote the boundary condition for coordinate points as A, B, C, and D.

$$\begin{cases} \Gamma(0, y_A, 0) = T_m - T_0, y_A > 0 \\ \Gamma(0, y_B, 0) = T_m - T_0, y_B < 0 \\ \Gamma(x_C, 0, 0) = T_m - T_0, x_C > 0 \\ \Gamma(x_D, 0, 0) = T_m - T_0, x_D < 0 \end{cases} \quad (21)$$

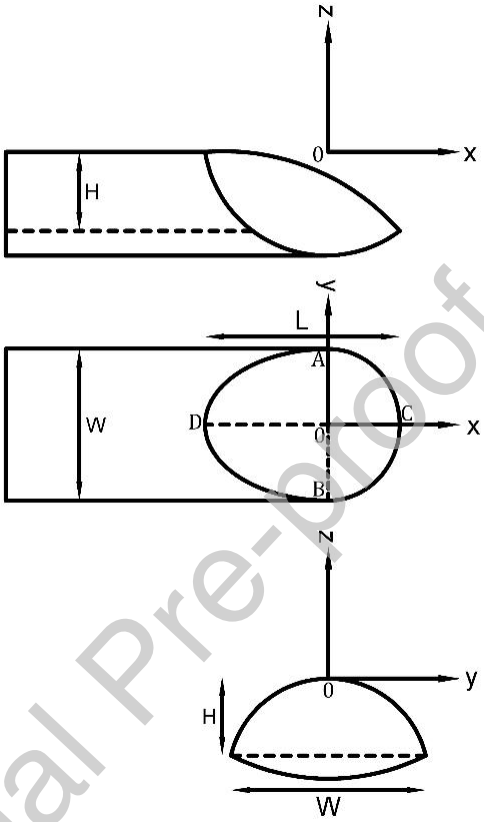

Figure 4. Schematic depiction of melt-pool projection on x-y, y-z, and x-z and planes (adopted from Ref. [24]).

The length (L) and width (W) of the melt-pool on the x-y plane according to the boundary are defined as:

$$L = x_C - x_D, W = 2|y_A| = 2|y_B| \quad (22)$$

To find the deposit height, the catchment efficiency needs to be defined. It can be defined as the area of the melt-pool projection on the x-y plane over the cross-sectional area of the powder stream column.

$$\eta = \frac{A_m}{A_{ps}} = \frac{\pi WL}{4\pi r_{ps}^2} \quad (23)$$

where, A_m can be found based on the boundary of the melt-pool projection on the x-y plane, and r_{ps} is the effective radius of the powder stream. Then, the deposit height can be found based on the conservation of mass (continuity). The mass flow rate through the melt-pool cross-sectional volume is constant. Assuming the cross-section of deposit on the y-z plane is a parabolic segment, the cross-sectional area would be:

$$A_d = \frac{2}{3}WH \qquad (24)$$

The powder mass flow rate injected to the melt-pool volume defines the height.

$$\eta F = \rho v A_d$$

$$\frac{\pi WL}{4\pi r_{ps}^2} F = \frac{2}{3}\rho v W H$$

$$H = \frac{3LF}{8\rho v r_{ps}^2} \qquad (25)$$

2.3. Determination of threshold-limits for the process mapping

2.3.1. Laser power needed for deposition

The power required to form a deposit with a specific width can be derived from Eq. 15. The equation can give the initial power given by the laser beam to form a deposit (P_{dep}) with a specific width. The boundary condition is that the temperature on the top surface at the coordinate of $(0, y, 0)$ is equal to the melting temperature of the deposit, where y can be the radius of the deposit with respect to the radius of the laser beam.

$$x = 0, z = 0, y = 2r_l; R = 2r_l$$

$$T_{dep} - T_0 = \frac{1}{2\pi kR}\left[P_{Total}^{Deposition}\right] e^{\frac{-v(R)}{2\alpha}}$$

$$2\pi kR(T_{dep}-T_0)e^{\frac{+v(R)}{2\alpha}}$$

$$= \beta_s P_{dep} exp\left(\frac{-\varepsilon F L_{att}}{A_{ps} v_p}\right) + \frac{N\beta_p A_p}{A_l v_p} P_{dep} \int_0^{L_{att}} exp\left(\frac{-\varepsilon F z}{A_{ps} v_p}\right) dz$$

$$+ \frac{N\beta_p A_p}{A_l v_p}(1-\beta_s) P_{dep} \int_0^{L_{att}} exp\left(\frac{-\varepsilon F z}{A_{ps} v_p}\right) dz \qquad (26)$$

2.3.2. Laser power needed to powder fusion

The particles should be melted before reaching the melt-pool; otherwise, the quality of the deposit is affected. Not only do non-melted and partially melted particles affect the stability of the deposition process but also they may help porosity formation. The accumulated energy by the particle by the time they reach the substrate is consumed to heat the particles. Here, to define this threshold for the initial laser power for powder fusion (P_{pf}), it is assumed that the energy absorbed by particles is completely consumed for particles' fusion.

$$\frac{N\beta_p A_p}{A_l v_p} P_{pf} \int_0^{L_{att}} exp\left(\frac{-\varepsilon F z}{A_{ps} v_p}\right) dz + \frac{N\beta_p A_p}{A_l v_p}(1-\beta_s) P_{pf} \int_0^{L_{att}} exp\left(\frac{-\varepsilon F z}{A_{ps} v_p}\right) dz$$

$$= N m_p c_p (T_{pf} - T_0) + N m_p L_f \qquad (27)$$

where c_p is the specific heat capacity of powder, and L_f is the latent heat of fusion.

2.3.3. Laser power needed to form a stable melt-pool

When the power density is too low or high, the material can be not melted or vaporized from the melt-pool. In the case of high power density, the generated heat can penetrate to a deeper depth, causing high dilution that is not desirable. On the other hand, the formation of a plasma in this condition is inevitable. When a strong plasma forms near the melt-pool, a considerable part of the laser-beam energy can be absorbed by the plasma before the beam reaches the material. This may deteriorate the process efficiency and quality of the deposits. Thus, it is important to define the threshold for material vaporization [36,37].

An analytical approach of utilizing normalized enthalpy has been effectively used to relate the vaporization threshold to the parameters of the laser processing. This method has been used by Hann et al. [38] and Fabbro [39] for laser welding, and King et al. [40] and Rubenchik et al. [41] expanded this method to laser additive manufacturing. The linear dependence of the normalized melt-pool depth to the normalized enthalpy has been shown in previous studies, where the enthalpy or energy density (ΔH) can be represented as the energy absorbed during the interaction time over the heat diffusion volume.

The heat diffusion volume for one-dimensional heat flow can be assumed as the volume of a cylinder. The section of the cylinder is assumed as a circle.

$$Diffusion\ volume = \pi {r_l}^2 \delta \tag{28}$$

$$\delta = \sqrt{\alpha t_i}$$

$$t_i = \frac{2r_l}{v}$$

where, r_l is the radius of the cylinder equals the effective laser beam radius and δ is the height of the cylinder equals the heat diffusion depth during the interaction time (t_i) for one-dimensional heat flow. With these assumptions, the energy density can be found as:

$$\Delta H = \frac{P_{Total}^{Deposition} t_i}{Diffusion\ volume} = \frac{\sqrt{2} P_{Total}^{Deposition}}{\pi \sqrt{\alpha v r_l^3}} \tag{29}$$

The normalized enthalpy is $\frac{\Delta H}{h_s}$, where ΔH is the specific enthalpy calculated above, h_s is the enthalpy at melting equals to $\rho c_p (T_m - T_0)$. The normalized enthalpy can be used to identify the thresholds where instabilities in melt-pool formation happen. The melt-pool instabilities, as defined by Hann et al. [38], happen when the enthalpy is smaller than enthalpy at melting and greater than enthalpy at vaporization. Hann et al. [38] showed that enthalpy at vaporization over enthalpy at melting is roughly equal to 10 for

most of metallic alloys. The assumption of $\frac{\Delta H}{h_s} = 10$ can define a threshold when the material vaporization starts to happen (P_{mv}). The assumption of $\frac{\Delta H}{h_s} = 1$ can similarly define another threshold when material fusion happens (P_{mf}).

3. Material and methods

Spherical plasma-atomized Ti-5Al-5V-5Mo-3Cr (Ti-5553) alloy powder (AP&C, GE Additive) with particle size ranged from 45 to 106 μm (shown in Figure 5) was deposited on the plates made of Ti-6Al-4V (Ti-64) alloy (McMaster-Carr) by an LDED-CPF setup (DMD®-IC106, DM3D Technology). The LDED-CPF system (shown in Figure 6) is equipped with an ABB robotic control system, a disk laser (TruDisk 2000, TRUMPF) with the maximum power of 2 KW and wavelength 1030 nm, and a dual powder feeder that is used to feed the metallic powder through a coaxial nozzle.

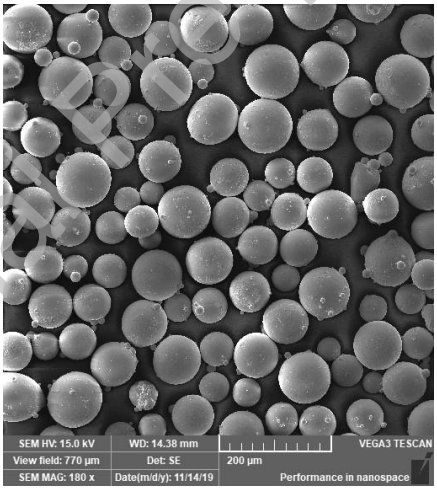

Figure 5. SEM image of the feedstock Ti-5553 powder.

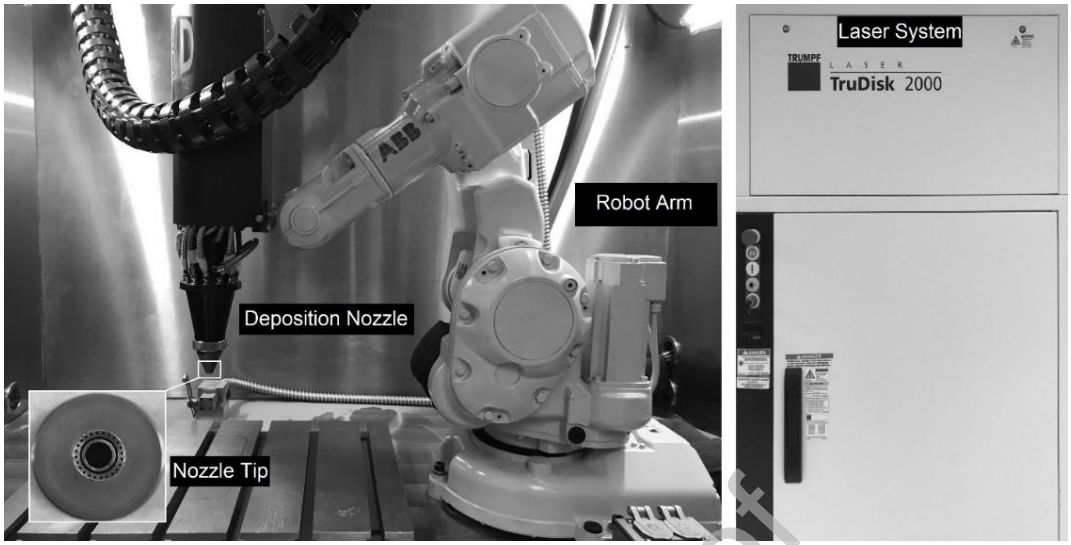

Figure 6. Robotic LDED-CPF equipment used in this study.

The thermal parameters of both substrate and feedstock powder (Table 1) are averaged out over the range of room to melting temperature as the thermophysical properties of materials are temperature-dependent. Single-track depositions were conducted at different laser power and carrier gas to validate the model. Each group experiment was repeated three times and the process parameters are listed in Table 2.

Table 1. Thermophysical properties of the materials

Material	Form	Melting Temperature [K]	Density [g/cm^3]	Thermal conductivity [W/m·K]	Specific heat [J/(g·K)]
Ti-5553	Powder	1923	4.3 (298 K)-3.4 (1923 K)	5 (298 K)-29 (1923 K)	0.53 (298 K)-0.75 (1923 K)
Ti-64	Plate	1928	4.4 (298 K)-3.9 (1928 K)	17 (298 K)-34 (1928 K)	0.57 (298 K)-0.85 (1928 K)

Table 2. Technical and processing parameters of LDED-CPF

Parameter	Value
Laser moving velocity	11 mm/s
Powder feed rate	14.5 g/min
Nozzle standoff distance	10 mm
Laser power	250, 500, 1000, 1500, 1750 W
Carrier gas flow rate (Argon)	1.1, 1.7, 4.7, 7.8, 9.3 L/min
Cover gas flow rate (Argon)	8 L/min

Nozzle gas flow rate (Argon+Helium)	6 and 4 L/min
Shaping gas flow rate (Argon)	6 L/min

The powder stream images were taken by a Canon EOS REBEL T7i60D camera equipped with a Canon EF 100mm F/2.8 Macro USM Lens. The powder stream luminance was analyzed by the gray-value tool of ImageJ software. The powder stream videos were taken by a high-speed camera (VEO 710, Phantom) equipped with a Canon EF 180mm F/3.5L Macro USM Lens. The average particles velocity was experimentally measured by the available tool of Phantom CineViewer (CV) software.

Kapton films with a thickness of 100 µm were used to determine the laser spot size. One pulsation of laser with the power of 60 W and a duration of 1 ms was used at different standoff distances to find the laser spot size at different distances from the nozzle tip. The burnt spots on the Kapton films were then measured by optical microscopy. Each beam condition was repeated four times for calculation of a mean and standard deviation. A portable power meter (PMT 05p, PRIMES GmbH) is used to measure the laser power. The attenuation of the laser beam by the powder cloud at different gas and powder parameters is investigated by the power meter. The power meter placed at the standoff distance, as the substrate, and the laser fired at a low laser power of 60 W for 20 seconds while the powder feeder was on.

To examine the geometry of the single-tracks, a laser scanning confocal microscope (VK-X250, Keyence) is used. All the single-track deposits were cross-sectioned at the mid-track length and then mounted, ground, polished and etched to investigate the microstructure by optical and scanning electron microscopy (VEGA3, TESCAN). The mathematical model is implemented in Matlab® R2019a by a DELL® computer with Intel® CoreTM i7-7700 CPU 3.6GHz.

4. Results and discussion

4.1. Particles velocity

Figure 7 shows the comparison of average particles velocity for the model-predicted values and experimental values based on different volumetric gas flow rates. The volumetric gas flow rates obtained by adding up the cover gas flow rate and carrier gas flow rate that is divided into 4 pipelines. The graph implies that the assumption of assuming the particles velocity equal to the gas flow rate speed is more or less valid. The difference can lie behind the effect of the drag force and the error of the measurements.

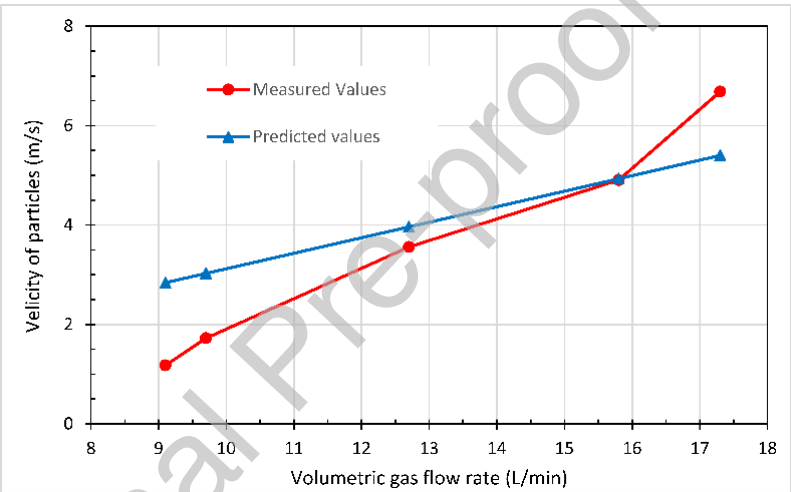

Figure 7. Experimental and model predicted values of particles velocity.

4.2. Powder stream

To express the powder distribution, the optical luminance analysis is a handy method verified by Pinkerton and Li [30]. The powder stream images were taken and the powder stream luminance was assessed by gray-value line profile tool (ImageJ Software). Figure 8 shows an example of this method to show the Gaussian distribution in transverse planes at different standoff distances. From the results of the gray-value line profile, the powder stream showed relatively the same distribution pattern and intensity within a standoff distance ranged from 8 to 12 mm. Thus, the focal position of the powder stream can be approximately in this range. The nozzle standoff distance from the substrate was set at 10 mm (in the

middle of the focal position range) and hence the attenuation length would be 2 mm. The powder particles come out of the annular outlet at different angles and converge in the focal position range. The average converge angle is 70 degree and the maximum powder concentration happens within the focal position range. Thus, for the sake of simplification, the assumption of the powder stream as a cylinder with the effective radius and the height of the focal position range is reasonable. In this study, the effective radius is considered as the distribution reaching $\frac{1}{e}$ of the peak concentration value. Thus, in a simple way, the powder stream is a cylinder with an effective radius of 2.8 mm and a height of 4 mm.

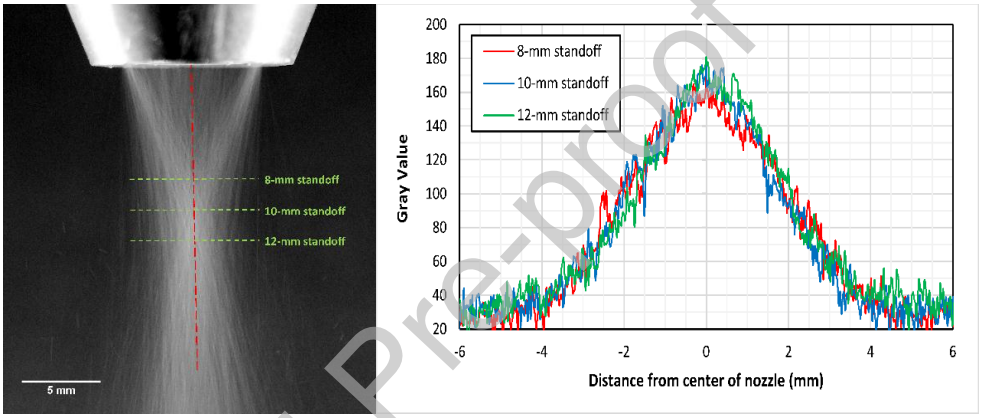

Figure 8. (a) Grayscale image of Ti-5553 powder stream taken at a powder flow rate of 6.5 g/min and carrier gas of 4 L/min (green dotted lines show the standoffs used for line profile measurement) (b) Measured gray value showing the powder distribution at different standoff distances.

4.3. Laser beam profile

The laser beam spot size on the focal position is a critical parameter in laser materials processing. Indirect measurement of the burnt contour on Kapton films is an easy and inexpensive method to determine the approximate laser beam spot size [42]. Depending on laser beam power intensity, the Kapton undergoes pyrolytic decomposition or vaporization, forming a distinct burnt contour that can be easily measured as an effective laser beam diameter. Figure 9 shows an example of this method expresses the laser spot size at different standoff distances.

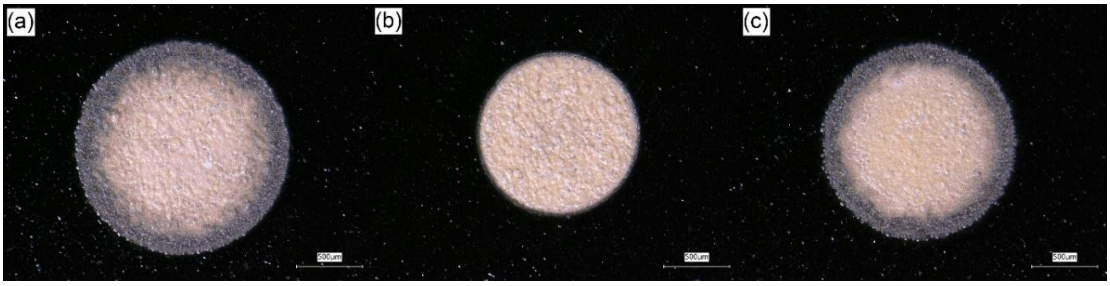

Figure 9. Burnt spot formed on the Kapton film at different distances from the nozzle tip; (a) 5 mm, (b) 15 mm, and (c) 25 mm.

Figure 10 shows the laser beam profile based on the measurements of burnt spots formed on the Kapton film at different distances from the nozzle tip. The waist of the beam is at a standoff distance of 15 mm, the beam radius at the waist is 0.6 mm, and the far-field divergence angle is 4.6°.

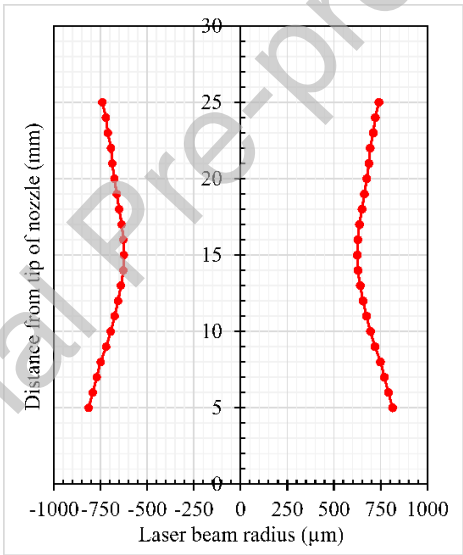

Figure 10. The laser beam profile based on the measurements on Kapton films.

4.4. Attenuation of laser beam intensity by powder cloud

Figure 11 shows the comparison of predicted and measured values of the attenuated laser power as a function of the particles velocity and powder feed rate. The maximum laser beam attenuation percentage is predicted around 8% at the highest powder feed rate (14.5 g/min) and lowest particles velocity (1.4 m/s). However, the graphs show some contradictory results between the measured and predicted values.

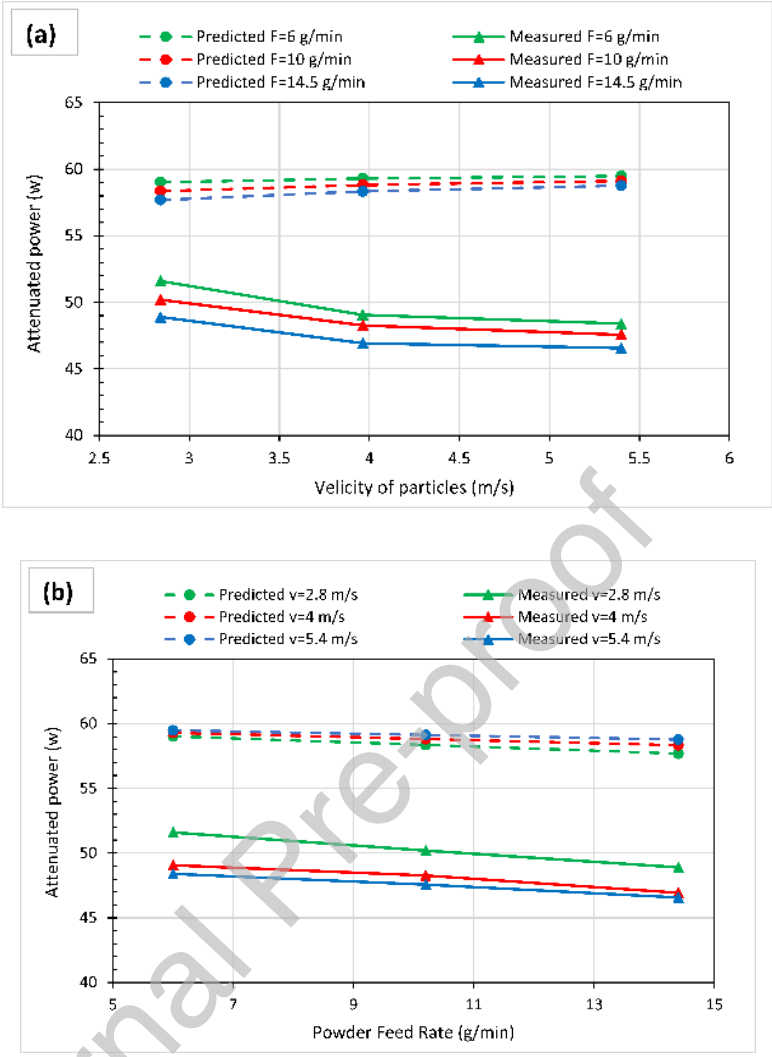

Figure 11. Attenuated laser power as a function of particles velocity (a) and powder feed rate (b).

The source of error could be attributed to the method of measurement. One of the main assumptions of the model is that the powder particles, interacted with the laser beam, are effectively attached to the liquid flow and become part of the melt-pool. However, at the low power used for the measurement, no melt-pool forms and particles hit the surface of the power meter and bounce back into the laser-beam column, double attenuating the laser power and cause the mismatch between predicted and measured values. Especially as the particles velocity increased, the mismatch becomes higher as particles with high velocity can bounce back a higher distance and attenuate the laser beam more.

4.5. Melt-pool/deposit temperature distribution

It is challenging to experimentally measure the precise temperature field due to the temperature measurement dependencies on nonlinear emissivity. The analytical model is an efficient approach to predict the temperature field in different sections and estimate the melt-pool geometry during the LDED-CPF process. Figure 12 shows the melt-pool temperature distribution based on the model implemented in Matlab. The melt-pool boundary is identified by the liquid-solid isotherm. The deposit bead curvature is defined based on the polynomial curve fitting to the data points of the width and height. The only drawback is the temperature prediction at the points close to $(0, 0, 0)$ position. The Rosenthal's solution is based on a point heat source and it results in the prediction of very high temperatures for those points. To deal with this, maximum temperature threshold should be defined and the area close to $(0, 0, 0)$ position ends up with the same temperature distribution; however, the temperature prediction at the points far from the $(0, 0, 0)$ position would be accurate enough.

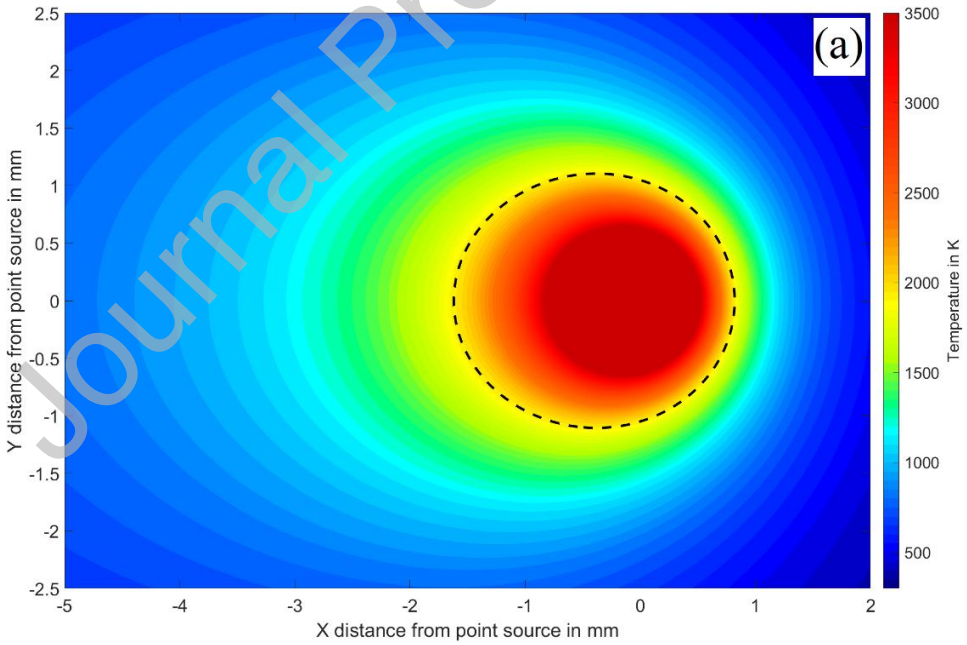

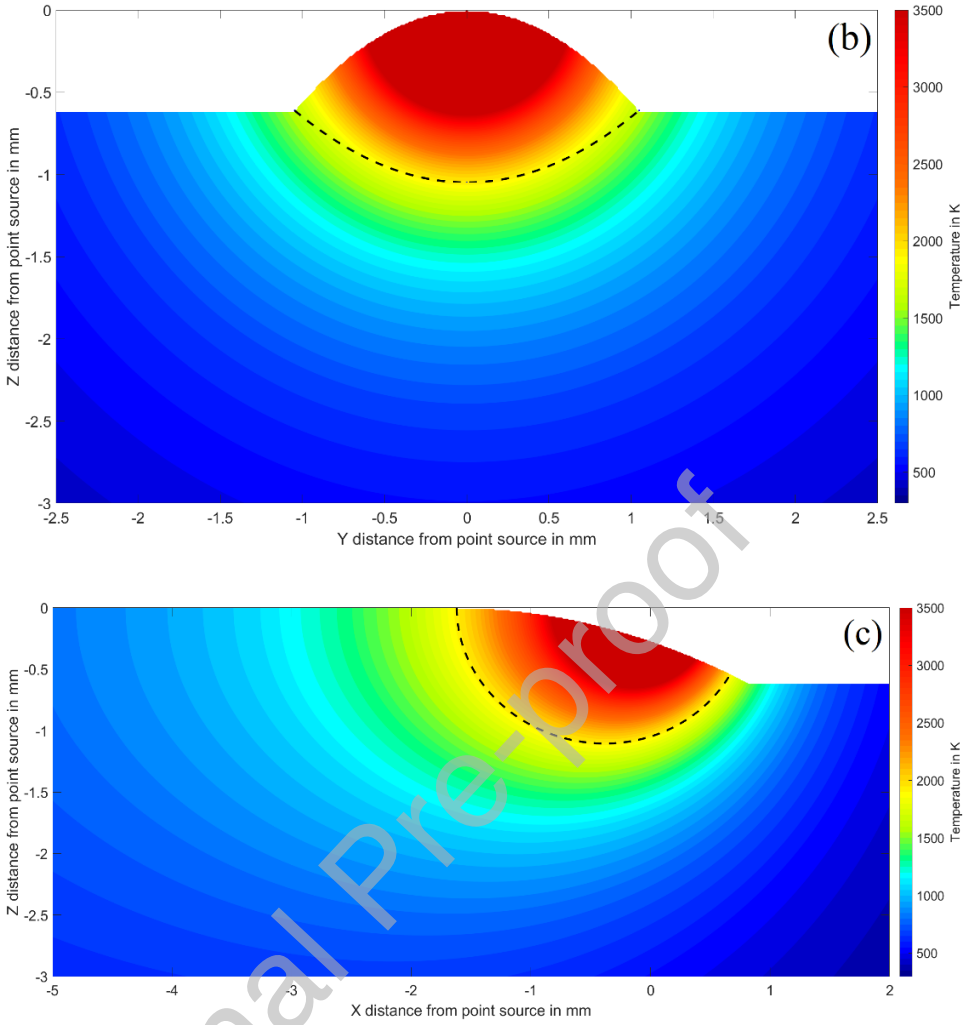

Figure 12. Melt-pool temperature field in different planes. (a) xy plane (substrate surface), (b) yz plane (transverse cross-section), (c) xz plane (longitudinal cross-section) (P=1000 W, $\dot{V}$=9.7 L/min, F=14.5 g/min and v=11 mm/s). The melt-pool boundary is indicated by the black dashed line (T=1931 K).

4.6. Deposit geometry

The geometrical features such as height and width are measured by a KEYENCE laser confocal microscope based on the transverse cross-section and 3D contour of the deposits. Figure 13 and Figure 14 show the transverse cross-section and 3D contour of the deposits at different laser powers.

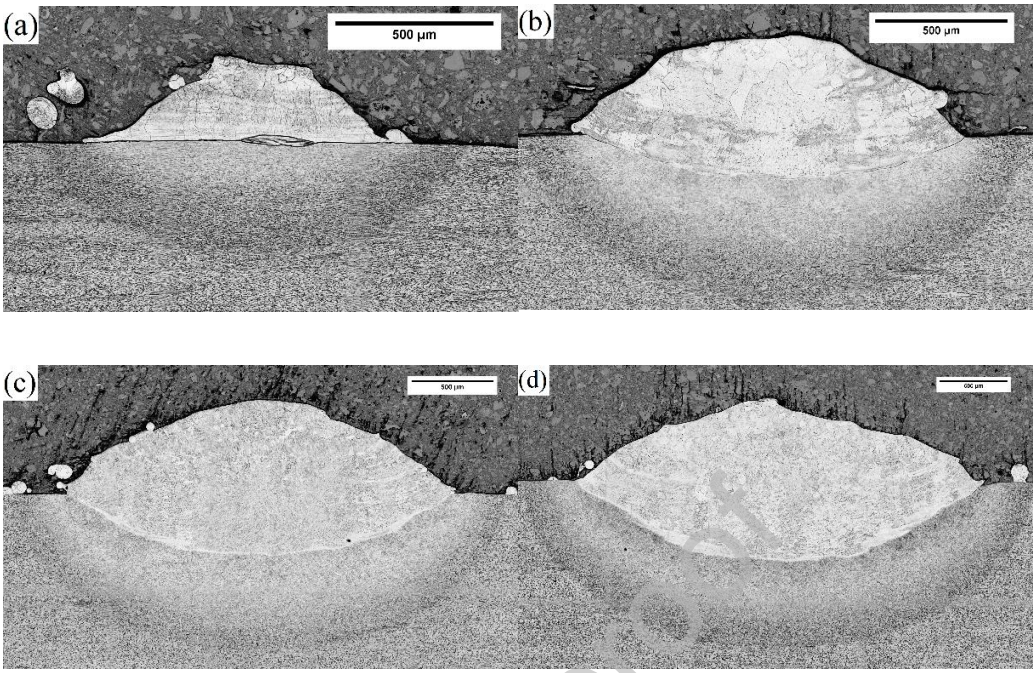

Figure 13. Transverse cross-section of deposits at different laser powers of (a) 250 W, (b) 500 W, (c) 1000 W, and (d) 1500 W ($\dot{V}$=9.7 L/min, F=14.5 g/min and v=11 mm/s).

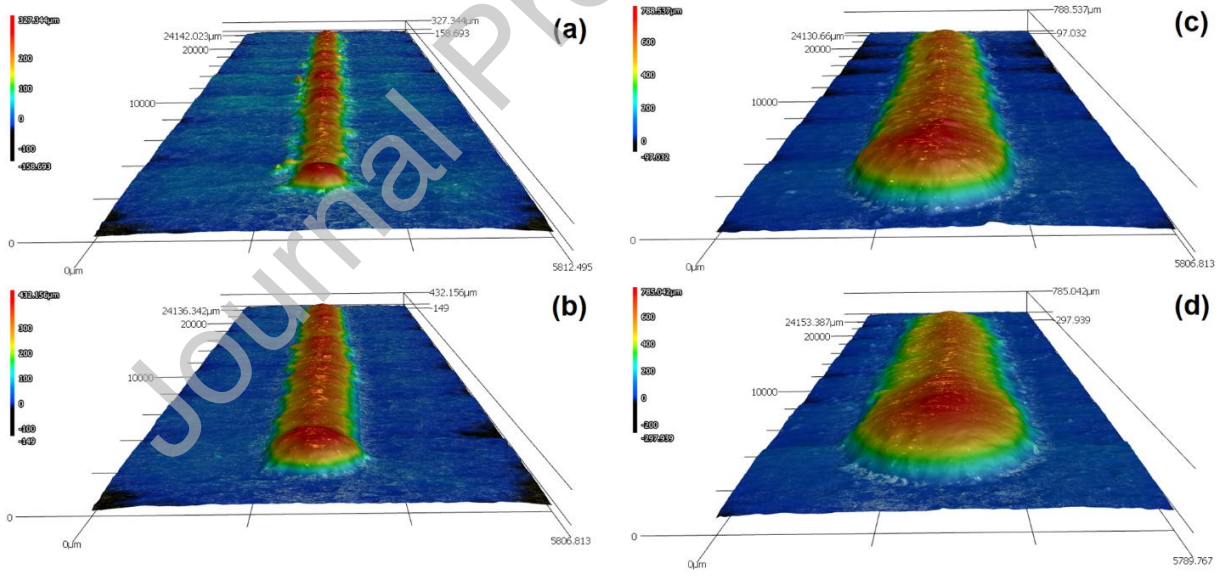

Figure 14. 3D contour of single deposits at different laser powers of (a) 250, (b) 500, (c) 1000, and (d) 1500 W ($\dot{V}$=9.7 L/min, F=14.5 g/min and v=11 mm/s).

Figure 15 compares the predicted and measured deposit geometry with varying laser power and carrier gas flow rate. The measured results have low standard deviation values and only average values are

plotted. The predicted values are more or less match with the measured ones. With increasing laser power, the deposit width, dilution, and height increase; however, the effect of carrier gas flow rate or particles velocity is negligible. It should be mentioned that the correction factor for the enhanced thermal conductivity is anisotropic and it may be different in different directions, usually greater in the depth direction than the in-plane direction [32–34]. In this work, the correction factor of thermal conductivity is assumed to be 2 to find the width of the melt-pool and 2.5 for finding the depth of the melt-pool. As the Marangoni effect is more pronounced in the z-axis, a larger correction factor should be considered for the melt-pool depth.

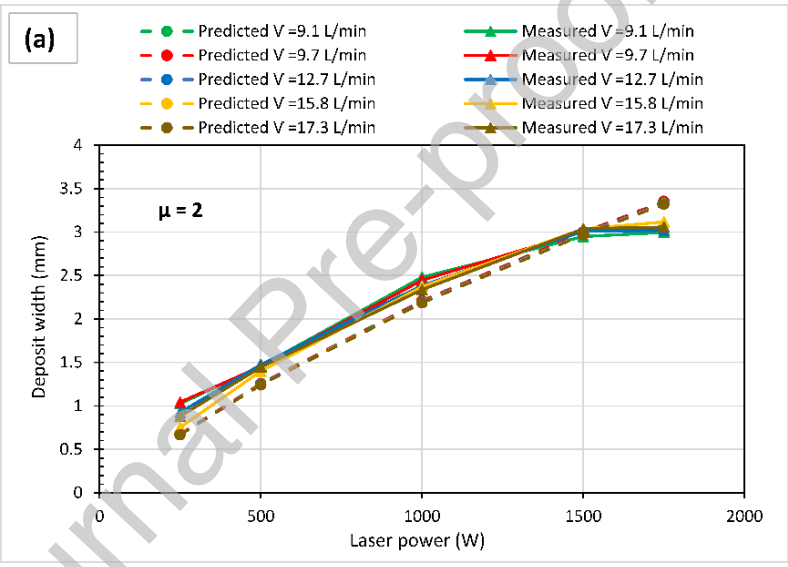

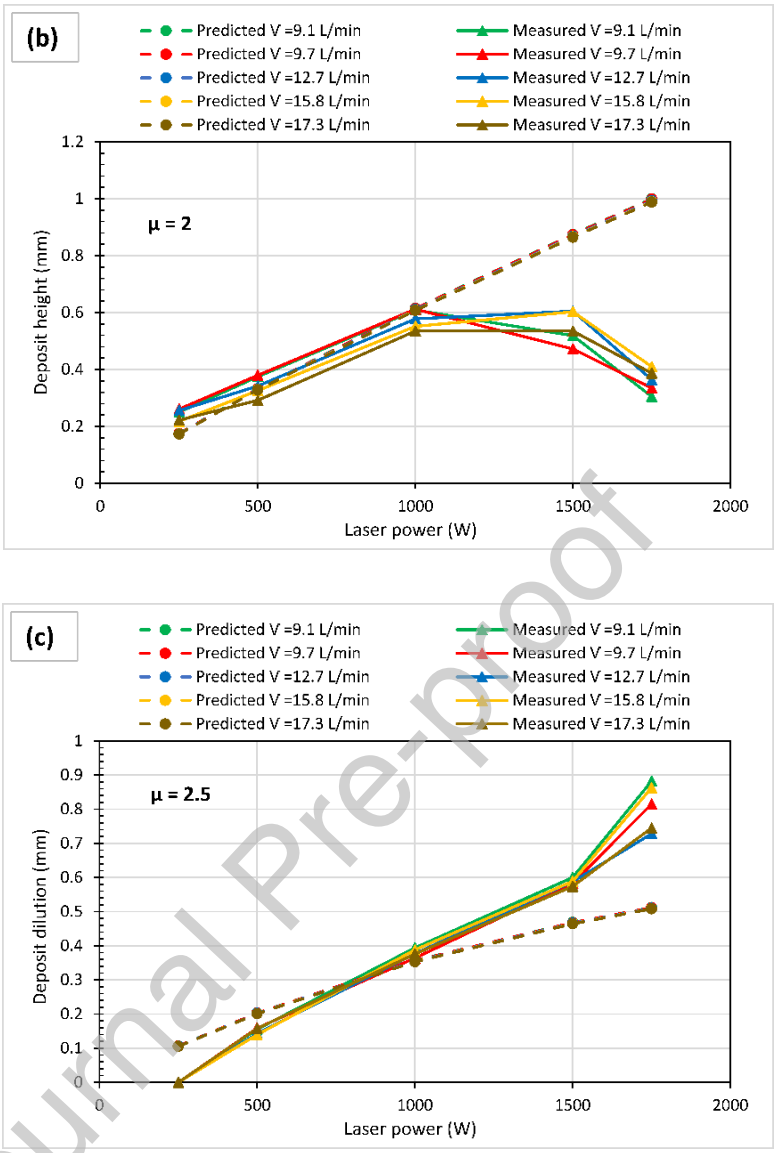

Figure 15. Measured and predicted values for the deposit geometry in different laser powers and carrier gas flow rates using two correction factors (μ) for the enhanced thermal conductivity (F=14.5 g/min and v=11 mm/s); (a) width (μ=2), (b) height (μ=2), and (c) dilution (μ=2.5).

The particles velocity has a minor effect since the attenuation time is very short. There is a small discrepancy between predicted and measured values, which is normal for an analytical model that entails several simplifications. The source of errors may attribute to the simplifications for considering the average thermophysical properties over the temperature range, ignoring the effect of gravity and drag force on particles velocity, and disregarding convection and radiation losses. Based on the measured

values, there are major discrepancies in the deposit geometry depending on the laser power. At laser power of 250 W, the relative error of predicted and measured values is high. The relative error is high in the case of laser powers of 1500 and 1750 W, too. At laser powers of 500 and 1000 W, the relative error for the height, dilution, and width is 5-20 %, which is acceptable for an analytical model. The source of errors may attribute to the governing physics that are not considered in the model. The first simplifying assumption is that the injected powder from the nozzle must completely be melted and attracted by the melt-pool. If this condition is not satisfied, the deposition process would be unstable, leading to a high discrepancy between the predicted and measured values. The second assumption is that the power density must be in range in order to ensure that stable melt-pool forms and the material is not vaporized. If this condition is not satisfied, a lack of fusion and vaporization would lead to a high discrepancy between predicted and measured values. The procedure for the determination of these threshold-limits is presented in the previous section and results are presented in the following section.

4.7. Developed process map

By implementing the model in Matlab, the different thresholds can be drawn for the LDED-CPF process. In Figure 16, the laser power is plotted as a function of particles velocity in the case of single-track depositing of Ti-5553 powder on Ti-64 plates. The black solid line shows the deposition power (P_{dep}) of forming a deposit with a specific width ($W = 2r_l$). The blue solid line show the required power of particles' fusion (P_{pf}) before they reach the melt-pool. The two red solid lines are the thresholds of forming a stable melt-pool. The first one is the required power for material fusion (P_{mf}) and the second one is power at which material vaporization starts to happen (P_{mv}). The intersections of these lines form different zones indicating different regimes for the LDED-CPF process. The zone below P_{pf} is not preferred as the particles have a temperature below the melting point and they may cause instability in the process. However, the deposition can be still done in the zones below P_{pf}, the results would not be desirable. Similarly, the zones below P_{mf} and above P_{mv} is not desirable since no stable melt-pool forms beyond them. The zone highlighted in green would be the optimal processing zone for LDED-CPF of Ti-

5553 (75 µm average size) on the Ti-64 substrate at the given powder feed rate and laser moving velocity and the geometry prediction of the model is valid with good accuracy. This figure clearly shows the crucial role of the laser power and particles velocity on defining the processing zone. The particles velocity has a minor effect on P_{dep}. However, it has a major effect on P_{pf}. In fact, P_{pf} increases linearly as the particles velocity increases.

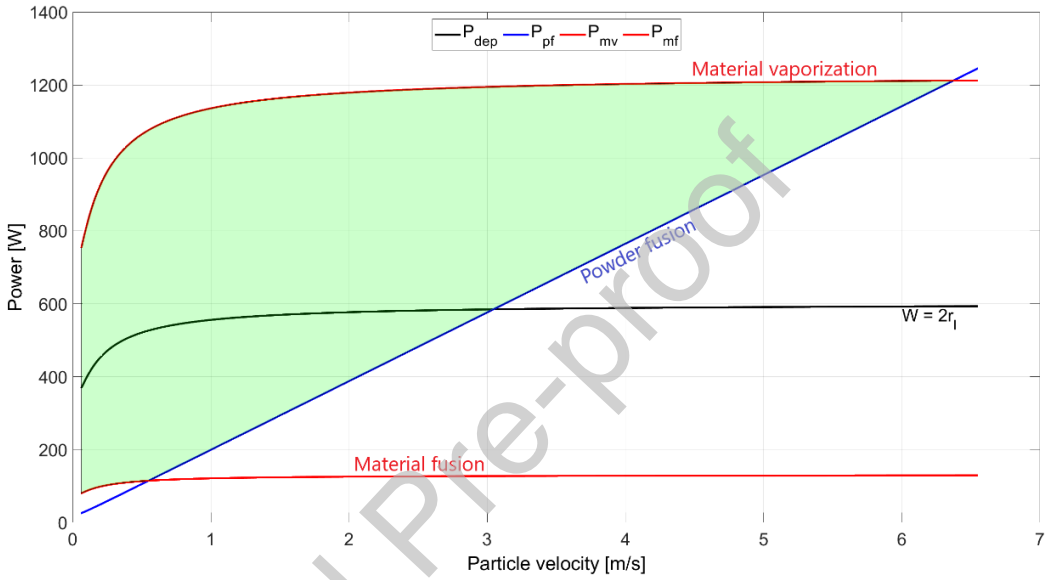

Figure 16. The modeled process map representing laser power versus particles velocity for LDED-CPF of Ti-5553 on the Ti-64 substrate (F=14.5 g/min and v=11 mm/s).

4.8. Microstructure of the deposits

Figure 17 shows the microstructure of single deposits that were fabricated at different laser powers when other processing conditions were kept constant. The single deposit printed at 250 W showed a dendritic structure of β-Ti phase (Figure 17a). However, increasing laser power tends to generate a martensitic α/β structure (Figure 17b-d).

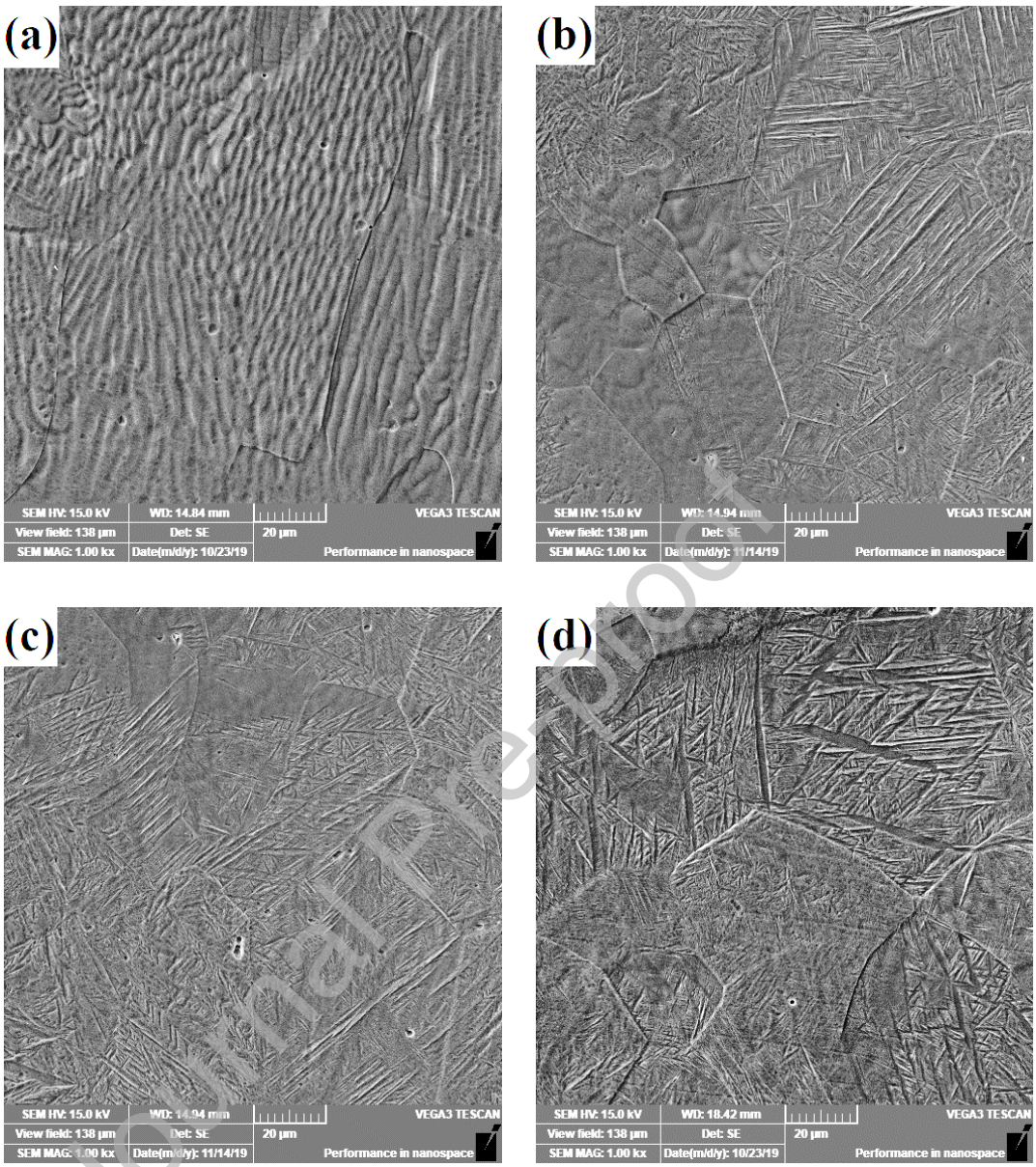

Figure 17. SEM micrographs for the typical microstructure in the Ti-5553 single deposits on Ti-64 substrate at different laser powers; (a) 250, (b) 500, (c) 1000, and (d) 1500 W ($\dot{V}$=9.7 L/min, F=14.5 g/min and v=11 mm/s).

The reason for this microstructural change lies behind the chemical composition change induced by dilution. As the laser power increases, the dilution level of deposit and substrate increases. The substrate is Ti-64 alloy with less β-stabilizing elements. The dilution decrease the molybdenum and chromium content of the deposits and leads to the martensitic α/β structure. The EDS results from the transverse cross-sectional area of the deposits (Table 3) confirm that the increased laser power and following

dilution decreases the molybdenum and chromium content. This finding can benefit the process. The first layers can be printed by the parameters that lead to less dilution such that the chemical composition remains untouched, especially in case using a substrate with different chemical composition as the powder, and the process can be continued by other processing parameters.

Table 3. Normalized mass concentration [%] of the deposits at different laser power obtained by EDS

	Titanium	Aluminum	Vanadium	Molybdenum	Chromium
Deposit at 250 W	81.18	5.26	5.86	5.99	1.70
Deposit at 500 W	83.81	5.81	5.64	3.51	1.23
Deposit at 1000 W	84.82	5.49	5.28	3.26	1.14
Deposit at 1500 W	85.85	5.67	5.41	2.25	0.82

5. Conclusions

A mathematical model of LDED-CPF was developed in this paper to couple the heat and mass transfer by the attenuated laser power and heated powder particles. The energy balance was considered with Rosenthal's solution for a moving heat source to obtain the temperature field and melt-pool geometry with some considerations such as the effect of fluid motion, the increased absorptivity by the angle of incidence, and the contribution of remelted/diluted zone to the melt pool's thermophysical properties. An alternative solution to calculate the deposit height was developed by considering the catchment efficiency based on real melt-pool size. A process map was developed to complete the model based on a few important phenomena to avoid problematic processing parameters.

The experimental validation was performed using the single-track deposition of Ti-5553 and it showed the accuracy of the model depends on the processing parameters. The non-optimized processing parameters led to the vaporization or lack of fusion, resulting in a high discrepancy in the results. Those non-optimum processing parameters were avoided by the process map. By identifying the optimal

processing region on the process map, the model is able to predict the geometry of the single-track deposits with more than 80% accuracy. This model gives general insights into the LDED-CPF process and can act as a guideline on the processing parameter selection that governs the major aspects of the process.

Acknowledgments

The authors would like to acknowledge the financial support of the Natural Sciences and Engineering Research Council of Canada (NSERC), and the Ontario Research Fund – Research Excellence (ORF-RE).

Declaration of interests

The authors declare that they have no known competing financial interests or personal relationships that could have appeared to influence the work reported in this paper.

References

[1] ASTM F2792-12a, Standard Terminology for Additive Manufacturing Technologies, (2012). doi:10.1520/F2792-12A.

[2] L. Costa, I. Felde, T. Réti, Z. Kálazi, R. Colaço, R. Vilar, B. Verő, A simplified semi-empirical method to select the processing parameters for laser clad coatings, Mater. Sci. Forum. 414–415 (2003) 385–394. doi:10.4028/www.scientific.net/MSF.414-415.385.

[3] S. Liu, R. Kovacevic, Statistical analysis and optimization of processing parameters in high-power direct diode laser cladding, Int. J. Adv. Manuf. Technol. 74 (2014) 867–878. doi:10.1007/s00170-014-6041-y.

[4] M. Barekat, R. Shoja Razavi, A. Ghasemi, Nd:YAG laser cladding of Co–Cr–Mo alloy on γ-TiAl substrate, Opt. Laser Technol. 80 (2016) 145–152. doi:10.1016/j.optlastec.2016.01.003.

[5] M. Ansari, R. Shoja Razavi, M. Barekat, An empirical-statistical model for coaxial laser cladding of NiCrAlY powder on Inconel 738 superalloy, Opt. Laser Technol. 86 (2016) 136–144. doi:10.1016/j.optlastec.2016.06.014.

[6] B. Bax, R. Rajput, R. Kellet, M. Reisacher, Systematic evaluation of process parameter maps for laser cladding and direct energy deposition, Addit. Manuf. 21 (2018) 487–494. doi:10.1016/j.addma.2018.04.002.

[7] M. Ansari, A. Mohamadizadeh, Y. Huang, V. Paserin, E. Toyserkani, Laser directed energy deposition of water-atomized iron powder: Process optimization and microstructure of single-tracks, Opt. Laser Technol. 112 (2019) 485–493. doi:10.1016/j.optlastec.2018.11.054.

[8] A. Dass, A. Moridi, State of the Art in Directed Energy Deposition: From Additive Manufacturing to Materials Design, Coatings. 9 (2019) 418. doi:10.3390/coatings9070418.

[9] A.J. Pinkerton, Advances in the modeling of laser direct metal deposition, J. Laser Appl. 27 (2015) S15001. doi:10.2351/1.4815992.

[10] I. Tabernero, A. Lamikiz, E. Ukar, L.N. López de Lacalle, C. Angulo, G. Urbikain, Numerical simulation and experimental validation of powder flux distribution in coaxial laser cladding, J. Mater. Process. Technol. 210 (2010) 2125–2134. doi:10.1016/j.jmatprotec.2010.07.036.

[11] O.B. Kovalev, D.V. Bedenko, A.V. Zaitsev, Development and application of laser cladding modeling technique: From coaxial powder feeding to surface deposition and bead formation, Appl. Math. Model. 57 (2018) 339–359. doi:10.1016/j.apm.2017.09.043.

[12] S.Y. Wen, Y.C. Shin, J.Y. Murthy, P.E. Sojka, Modeling of coaxial powder flow for the laser direct deposition process, Int. J. Heat Mass Transf. 52 (2009) 5867–5877. doi:10.1016/j.ijheatmasstransfer.2009.07.018.

[13] E. Toyserkani, A. Khajepour, S. Corbin, Three-dimensional finite element modeling of laser

cladding by powder injection: Effects of powder feedrate and travel speed on the process, J. Laser Appl. 15 (2003) 153–160. doi:10.2351/1.1585087.

[14] E. Toyserkani, A. Khajepour, S. Corbin, 3-D finite element modeling of laser cladding by powder injection: effects of laser pulse shaping on the process, Opt. Lasers Eng. 41 (2004) 849–867. doi:10.1016/S0143-8166(03)00063-0.

[15] J.T. Hofman, D.F. de Lange, B. Pathiraj, J. Meijer, FEM modeling and experimental verification for dilution control in laser cladding, J. Mater. Process. Technol. 211 (2011) 187–196. doi:10.1016/j.jmatprotec.2010.09.007.

[16] S. Safdar, A.J. Pinkerton, L. Li, M.A. Sheikh, P.J. Withers, An anisotropic enhanced thermal conductivity approach for modelling laser melt pools for Ni-base super alloys, Appl. Math. Model. 37 (2013) 1187–1195. doi:10.1016/j.apm.2012.03.028.

[17] X. He, J. Mazumder, Transport phenomena during direct metal deposition, J. Appl. Phys. 101 (2007) 053113. doi:10.1063/1.2710780.

[18] H. Qi, J. Mazumder, H. Ki, Numerical simulation of heat transfer and fluid flow in coaxial laser cladding process for direct metal deposition, J. Appl. Phys. 100 (2006) 024903. doi:10.1063/1.2209807.

[19] M. Picasso, C.F. Marsden, J.D. Wagniere, A. Frenk, M. Rappaz, A simple but realistic model for laser cladding, Metall. Mater. Trans. B. 25 (1994) 281–291. doi:10.1007/BF02665211.

[20] A. Frenk, M. Vandyoussefi, J.-D. Wagnière, W. Kurz, A. Zryd, Analysis of the laser-cladding process for stellite on steel, Metall. Mater. Trans. B. 28 (1997) 501–508. doi:10.1007/s11663-997-0117-0.

[21] C. Lalas, K. Tsirbas, K. Salonitis, G. Chryssolouris, An analytical model of the laser clad geometry, Int. J. Adv. Manuf. Technol. 32 (2006) 34–41. doi:10.1007/s00170-005-0318-0.

[22] A.J. Pinkerton, R. Moat, K. Shah, L. Li, M. Preuss, P.J. Withers, A verified model of laser direct metal deposition using an analytical enthalpy balance method, in: Int. Congr. Appl. Lasers Electro-Optics, Laser Institute of America, 2007: p. 1806. doi:10.2351/1.5061038.

[23] S. Zhu, W. Chen, L. Ding, X. Zhan, Q. Chen, A mathematical model of laser cladding repair, Int. J. Adv. Manuf. Technol. (2019). doi:10.1007/s00170-019-03588-3.

[24] Y. Huang, M.B. Khamesee, E. Toyserkani, A comprehensive analytical model for laser powder-fed additive manufacturing, Addit. Manuf. 12 (2016) 90–99. doi:10.1016/j.addma.2016.07.001.

[25] J.M. Jouvard, D.F. Grevey, F. Lemoine, A.B. Vannes, Continuous wave Nd:YAG laser cladding modeling: A physical study of track creation during low power processing, J. Laser Appl. 9 (1997) 43–50. doi:10.2351/1.4745444.

[26] U. de Oliveira, V. Ocelík, J.T.M. De Hosson, Analysis of coaxial laser cladding processing conditions, Surf. Coatings Technol. 197 (2005) 127–136. doi:10.1016/j.surfcoat.2004.06.029.

[27] M. Kubiak, W. Piekarska, Z. Saternus, S. Stano, Numerical modelling of thermal and structural phenomena in Yb:YAG laser butt-welded steel elements, Arch. Metall. Mater. 60 (2015) 821–828. doi:10.1515/amm-2015-0213.

[28] N. Yang, Concentration model based on movement model of powder flow in coaxial laser cladding, Opt. Laser Technol. 41 (2009) 94–98. doi:10.1016/j.optlastec.2008.03.008.

[29] J. Lin, Concentration mode of the powder stream in coaxial laser cladding, Opt. Laser Technol. 31 (1999) 251–257. doi:10.1016/S0030-3992(99)00049-3.

[30] A.J. Pinkerton, L. Li, Modelling Powder Concentration Distribution From a Coaxial Deposition Nozzle for Laser-Based Rapid Tooling, J. Manuf. Sci. Eng. 126 (2004) 33. doi:10.1115/1.1643748.

[31] E. Toyserkani, A. Khajepour, S. Corbin, Laser Cladding, CRC Press, Boca Raton, 2004.

[32] C. Lampa, A.F.H. Kaplan, J. Powell, C. Magnusson, An analytical thermodynamic model of laser welding, J. Phys. D. Appl. Phys. 30 (1997) 1293–1299. doi:10.1088/0022-3727/30/9/004.

[33] W. Zhang, C.-H. Kim, T. DebRoy, Heat and fluid flow in complex joints during gas metal arc welding—Part II: Application to fillet welding of mild steel, J. Appl. Phys. 95 (2004) 5220–5229. doi:10.1063/1.1699486.

[34] T. Lienert, T. Siewert, S. Babu, V. Acoff, eds., ASM Handbook, Volume 6A: Welding Fundamentals and Processes, ASM International, Materials Park, Ohio, 2011.

[35] W.M. Steen, J. Mazumder, Laser Material Processing, 4th Edition, Springer London, London, 2010. doi:10.1007/978-1-84996-062-5.

[36] T. DebRoy, S.A. David, Physical processes in fusion welding, Rev. Mod. Phys. 67 (1995) 85–112. doi:10.1103/RevModPhys.67.85.

[37] R. Rai, J.W. Elmer, T.A. Palmer, T. DebRoy, Heat transfer and fluid flow during keyhole mode laser welding of tantalum, Ti–6Al–4V, 304L stainless steel and vanadium, J. Phys. D. Appl. Phys. 40 (2007) 5753–5766. doi:10.1088/0022-3727/40/18/037.

[38] D.B. Hann, J. Iammi, J. Folkes, A simple methodology for predicting laser-weld properties from material and laser parameters, J. Phys. D. Appl. Phys. 44 (2011) 445401. doi:10.1088/0022-3727/44/44/445401.

[39] R. Fabbro, Scaling laws for the laser welding process in keyhole mode, J. Mater. Process. Technol. 264 (2019) 346–351. doi:10.1016/j.jmatprotec.2018.09.027.

[40] W.E. King, H.D. Barth, V.M. Castillo, G.F. Gallegos, J.W. Gibbs, D.E. Hahn, C. Kamath, A.M. Rubenchik, Observation of keyhole-mode laser melting in laser powder-bed fusion additive manufacturing, J. Mater. Process. Technol. 214 (2014) 2915–2925. doi:10.1016/j.jmatprotec.2014.06.005.

[41] A.M. Rubenchik, W.E. King, S.S. Wu, Scaling laws for the additive manufacturing, J. Mater. Process. Technol. 257 (2018) 234–243. doi:10.1016/j.jmatprotec.2018.02.034.

[42] Z.Y. Wang, J.T. Liu, D.M. Hirak, D.C. Weckman, H.W. Kerr, Determining the Spot Size and Gaussian Distribution Coefficient of Pulsed Laser Beams Using KAPTON Films, J. Laser Appl. 5 (1993) 5–12. doi:10.2351/1.4745318.

Graphical Abstract